

# Topological Semimetal driven by Strong Correlations and Crystalline Symmetry

Lei Chen<sup>1</sup>, Chandan Setty<sup>1</sup>, Haoyu Hu<sup>1</sup>, Maia G. Vergniory<sup>2,3</sup>, Sarah E. Grefe<sup>4</sup>, Andrey Prokofiev<sup>5</sup>, Silke Paschen<sup>5,1,\*</sup>, Jennifer Cano<sup>6,7,\*</sup>, and Qimiao Si<sup>1,\*</sup>

<sup>1</sup>Department of Physics and Astronomy, Rice Center for Quantum Materials, Rice University, Houston, Texas 77005, USA

<sup>2</sup>Max Planck Institute for Chemical Physics of Solids, 01309 Dresden, Germany

<sup>3</sup>Donostia International Physics Center, P. Manuel de Lardizabal 4, 20018 Donostia-San Sebastian, Spain

<sup>4</sup>Theoretical Division, Los Alamos National Laboratory, Los Alamos, New Mexico 87545, USA

<sup>5</sup>Institute of Solid State Physics, Vienna University of Technology, Wiedner Hauptstr. 8-10, 1040 Vienna, Austria

<sup>6</sup>Department of Physics and Astronomy, Stony Brook University, Stony Brook, NY 11794, USA

<sup>7</sup>Center for Computational Quantum Physics, Flatiron Institute, New York, NY 10010, USA

**Electron correlations amplify quantum fluctuations and, as such, they have been recognized as the origin of a rich landscape of quantum phases. Whether and how they lead to gapless topological states is an outstanding question, and a framework that allows for determining novel phases and identifying new materials is in pressing need. Here we advance a general approach, in which strong correlations<sup>1,2</sup> cooperate with crystalline symmetry<sup>3,4</sup> to drive gapless topological states. We test this design principle by exploring Kondo lattice models and materials whose space group symmetries may promote different kinds of electronic degeneracies, with a particular focus on square-net systems. Weyl-Kondo nodal-line semimetals – with nodes pinned to the Fermi energy – are identified in both two and three dimensions. We apply the approach to identify materials for the realization of these correlation-driven topological semimetal phases. Our findings illustrate the potential of the proposed design principle to guide the search for new topological phases and materials in a broad range of strongly correlated systems.**

E-mails: qmsi@rice.edu; jennifer.cano@stonybrook.edu; paschen@ifp.tuwien.ac.at

Electron correlations and topology are well established as engines for surprising and potentially functional properties. Strong correlations promote quantum fluctuations, which engender abundant phases of matter and various quantum phase transitions<sup>1,2</sup>. Meanwhile, extensive developments have taken place in noninteracting electron systems, especially those with sizable spin-orbit couplings (SOC). In particular, the role of space group symmetry in determining and classifying symmetry-protected topological phases has been highlighted<sup>4-8</sup> and has led to a large materials database. We can expect that the intersection of these two fields will be especially fertile in breeding novel quantum phases, but it remains a largely open terrain especially for the case with gapless bulk excitations<sup>2,9</sup>. The usual approach starts from noninteracting symmetry-protected topological states. It considers the interactions as a perturbation<sup>10-12</sup>, or as producing a symmetry-breaking ordered state – such as a magnetic order – that in turn modifies the weakly-correlated topology<sup>3</sup>. In the opposite limit, where the correlations dominate over the kinetic energy, strongly correlated topological matter may arise. Until recently, no such strongly correlated gapless topological materials have been identified. It is pressing to realize concrete systems of this type, which are important in their own right and may also serve as anchoring points to explore the overall landscape of strongly correlated topological matter. Recently, a non-perturbative study in a strong-coupling limit has led to a Weyl-Kondo semimetal phase<sup>13-15</sup> on the diamond lattice. Concurrently, such a phase was advanced experimentally in a semimetallic cubic heavy fermion compound  $\text{Ce}_3\text{Bi}_4\text{Pd}_3$ <sup>16-18</sup>. The interplay between significant electron correlations and lattice geometry is also being explored experimentally in other materials such as the kagome metals<sup>19-21</sup>.

These developments motivate the search for a general non-perturbative framework to treat the interplay of correlation and topology and design strongly correlated gapless topological phases and materials. Our hypothesis is that strong correlations cooperate with crystalline symmetry to produce such states, as illustrated in Fig. 1(a). The proposed cooperation is counter-intuitive, because strong correlations tend to cause localization and gap out electronic excitations<sup>22,23</sup>. If validated, the proposition provides a design principle for identifying new strongly correlated gapless topological phases and materials.

To test this approach, it is important to go beyond the simplest model on the diamond lattice – a kind of “hydrogen atom” model of nodal fermions in three dimensions (3D)<sup>24</sup>. Thus we explore correlated systems with general space group symmetries that may promote different types of nodal electronic states and explore the possibility of realizing any new phases and materials in a same space-group symmetry. We narrow down the choice of strong-coupling models for

our study as follows. We focus on space group symmetries where electronic degeneracies may develop at partial fillings, regardless of orbital content. These often happen in nonsymmorphic space groups. We restrict ourselves to the case where interactions do not break crystalline or time-reversal symmetries, as a point of principle.

We thus consider a Kondo lattice system that contains nonsymmorphic mirror symmetry, which is known to favor Weyl nodal lines in noninteracting systems<sup>25–28</sup>. Furthermore, we focus on the nonsymmorphic and noncentrosymmetric square-net systems, which host both mirror and screw nonsymmorphic symmetries [Fig. 1(b)(c)]. We thus start from space group (SG) 129, which has been a fertile setting for electronic degeneracies of noninteracting systems<sup>29–34</sup> and is particularly advantageous in that the degeneracies are orbital-independent. We demonstrate the cooperation of strong correlations with space-group symmetry in producing a novel phase – a Weyl-Kondo nodal-line semimetal. Furthermore, we advance new candidate square-net materials to realize such correlation-driven topological semimetals.

We first focus on the simpler case of two dimensions (2D). This corresponds to the layer group  $p4/nmm$  which, when stacked in the  $z$ -direction, is described by the SG 129 ( $P4/nmm$ ). The Hamiltonian takes the form of a periodic Anderson model (PAM),  $\mathcal{H} = \mathcal{H}_d + \mathcal{H}_{cd} + \mathcal{H}_c$  (see Methods). Here, the  $d$ -fermion represents the physical localized  $f$  electrons, while the  $c$ -fermion denotes the light  $spd$  conduction electrons. The Hamiltonian of the spin-1/2  $d$ -fermions,  $\mathcal{H}_d$ , contains two parameters, the energy level  $E_d$  and onsite Coulomb repulsion  $U$ . The hybridization term,  $\mathcal{H}_{cd}$ , describes a coupling  $V$  between the spin-1/2 conduction  $c$ -fermion and the local  $d$ -fermion. The Hamiltonian of the conduction  $c$ -fermion,  $\mathcal{H}_c$ , is described in a matrix form:  $\mathcal{H}_c = \sum_{\mathbf{k}} \Psi_{\mathbf{k}}^\dagger H_c(\mathbf{k}) \Psi_{\mathbf{k}}$ , where  $\Psi_{\mathbf{k}}^T = (c_{\mathbf{k}\uparrow A}, c_{\mathbf{k}\downarrow A}, c_{\mathbf{k}\uparrow B}, c_{\mathbf{k}\downarrow B})$ , with  $A$  and  $B$  being the two sublattices,  $\mathbf{k}$  the wavevector, and  $\sigma = \uparrow, \downarrow$  marking the spin quantum numbers. It contains tight-binding hopping terms between the nearest ( $t_1$ ) and next-nearest ( $t_2$ ) neighbors, an SOC ( $t^{SO}$ ) term, and an inversion-symmetry-breaking ( $\Delta$ ) term. We focus on the case of quarter filling, corresponding to one electron per site. The saddle-point analysis of the effect of strong correlations is described in the Supplementary Information.

There is no Kondo effect when the hybridization strength is below a threshold value. In that case, all the electrons prefer to occupy the low-lying  $d$ -states to half filling, making the  $d$ -component to be a Mott insulator. Concomitantly, the conduction  $c$ -electron bands are completely empty, *i.e.* they lie above the Fermi energy. Fig. 2(a) shows the bandstructure for the case of the inversion-symmetry-breaking potential  $\Delta = 0$ , *i.e.* in the presence of the full  $p4/nmm$  symme-

try. The bands are generically two-fold degenerate. However, a four-fold degeneracy at  $X$  arises as a result of either the mirror nonsymmorphic  $\{M_z|\frac{1}{2}\frac{1}{2}\}$  symmetry or the screw nonsymmorphic  $\{C_{2x}|\frac{1}{2}0\}$  symmetry. The same degeneracy appears at  $Y$ , due to either the mirror nonsymmorphic  $\{M_z|\frac{1}{2}\frac{1}{2}\}$  symmetry or the screw nonsymmorphic  $\{C_{2y}|0\frac{1}{2}\}$  symmetry. Finally, a four-fold degeneracy also develops at  $M$ , from either the  $\{C_{2x}|\frac{1}{2}0\}$  or the  $\{C_{2y}|0\frac{1}{2}\}$  symmetry. Since these Dirac points occur far above the Fermi energy, they leave the ground state topologically trivial.

The Kondo effect develops when the hybridization goes above the threshold value. It generates composite fermions that must be located near the Fermi energy. Fig. 3(a) shows the renormalized dispersion for  $\Delta = 0$ . Because the composite fermion bands are subject to the same nonsymmorphic symmetry constraint, they also feature Dirac nodes at  $X$ ,  $Y$  and  $M$ . For the case of nonzero  $\Delta$ , *i.e.* when the inversion-symmetry is broken and the space group is reduced from SG 129 to SG 31, we show the renormalized dispersion in Fig. 3(b). The four-fold degenerate states at  $X$  and  $Y$  are split into two pairs of two-fold Weyl nodes above and below the Fermi energy. The different branches of the Weyl nodes cross each other at the Fermi energy, giving rise to Fermi-energy-bound Weyl-nodal lines, as shown in Fig. 3(c). The Weyl-nodal lines are protected by the mirror nonsymmorphic symmetry<sup>29,35</sup>. We note that the Kondo-driven nodal lines have been identified in the presence of SOC.

We next turn to the 3D case. To be definite, we consider  $\mathcal{AA}$  stacking of square-net layers as illustrated in Fig. 1(d), with the two stacking layers respectively hosting  $s$  and  $p$  orbitals<sup>26,27</sup>. In the PAM,  $\mathcal{H} = \mathcal{H}_d + \mathcal{H}_{cd} + \mathcal{H}_c$  (see Methods), with  $\mathcal{H}_d$  and  $\mathcal{H}_{cd}$  having the same form as before (except that the site summation is in the 3D lattice); they still contain three parameters: the  $d$ -electron energy level  $E_d$ , the on-site Coulomb repulsion  $U$  and the hybridization coupling  $V$ . For the conduction  $c$ -fermions, the Hamiltonian now takes the form:  $\mathcal{H}_c^{3D} = \sum_{\mathbf{k}} \Phi_{\mathbf{k}}^\dagger H_c^{3D}(\mathbf{k}) \Phi_{\mathbf{k}}$ , where  $\Phi_{\mathbf{k}}^T = (c_{\mathbf{k}\uparrow A}^s, c_{\mathbf{k}\downarrow A}^s, c_{\mathbf{k}\uparrow B}^s, c_{\mathbf{k}\downarrow B}^s, c_{\mathbf{k}\uparrow A}^p, c_{\mathbf{k}\downarrow A}^p, c_{\mathbf{k}\uparrow B}^p, c_{\mathbf{k}\downarrow B}^p)$ . In this equation,

$$\begin{aligned}
H_c^{3D}(\mathbf{k}) = & H_c(k_x, k_y) \otimes \rho_z + \Delta_z \rho_z + t_z^1 \sin\left(\frac{k_z}{2}\right) \rho_y \\
& + t_z^2 \cos(k_z) \rho_z + m_z \tau_x \otimes \sigma_x \otimes \rho_y,
\end{aligned} \tag{1}$$

with  $\rho_{x,y,z}$  being the Pauli matrices in the space of the two stacking layers. Here, the third and the fourth terms represent the nearest- and next-nearest-neighbor hoppings along the  $z$ -direction and the fifth term is the SOC along the  $z$ -direction. Again we focus on the quarter-filling case. When there is no Kondo effect, the conduction-electron bandstructure is shown in Fig. 2(b).

The Kondo effect also produces new composite fermions near the Fermi energy here, as shown

in Fig. 4(a). Nodal excitations develop in the dispersion of these composite fermions, which are more clearly seen in Fig. 4(b) as we zoom in to the immediate vicinity of the Fermi energy. In our model, they are precisely at  $E_F$ . These electronic degeneracies appear in the form of Weyl-nodal lines in the  $k_z = 0$  plane, as shown in Fig. 4(c). All these reflect the mirror nonsymmorphic  $\{M_z | \frac{1}{2} \frac{1}{2} 0\}$  symmetry. Because they are associated with the highly renormalized composite fermions, the Weyl nodal-line excitations have strongly reduced velocities. Here again, we stress that the nodal lines are robust against the SOC.

The realization of the Weyl-Kondo nodal-line semimetal in 3D is particularly important, as it suggests the emergence of drumhead surface states. We have computed the excitation spectrum on the (001) face in a slab with 40 unit cells. As indicated in Fig. 4(d), we find Kondo-driven drumhead surface states that are bounded by the projections of the Weyl rings. Importantly, the dispersion of the drumhead states also captures the Kondo energy scale and, hence, is strongly correlation-renormalized.

We now discuss some general lessons drawn from our results. Our models have an even number of electrons per unit cell. The typical localizing tendency of strong correlations could have turned the system into a Kondo insulator<sup>36–38</sup>. Instead, the strong correlations end up cooperating with the space-group symmetries, leading to Weyl-Kondo nodal-line semimetal phase.

To further underscore how this cooperation develops, we note that strong correlations typically produce emergent excitations *at low energies*. In our case, the Kondo effect generates composite fermions that are pinned to the immediate vicinity of the Fermi energy, within an energy window of  $k_B T_K$  (here  $T_K$  is the Kondo temperature). The space-group symmetry constrains these emergent excitations as well, leading to the emergent Weyl nodal excitations. While the fact that the nodal lines appear exactly at the Fermi energy in our model requires the added ingredient of particular fillings, the proximity of the Kondo-driven nodal lines to the Fermi energy, within the energy window  $k_B T_K$ , is to be expected for generic fillings.

We now turn to the experimental signatures of the Kondo-driven nodal-line Weyl semimetals. The first category of the signatures bear similarities with those of the Weyl-Kondo semimetals<sup>13–18</sup>. For example, because the velocity  $v^*$  is highly reduced from the typical bare conduction-electron value  $v$ , the specific heat has a quadratic temperature dependence with a large enhancement factor (see Supplementary Information):

$$c_v = \Gamma T^2. \quad (2)$$

Here, the prefactor is  $\Gamma = \frac{K}{2\pi} \frac{9\zeta(3)}{2} \left(\frac{k_B}{\hbar v^*}\right)^2 k_B$ , where  $K$  is the length of the nodal line and the zeta

function  $\zeta(3) \approx 1.202$ . It is enhanced from the typical noninteracting value by  $(v/v^*)^2$ , which is of the order  $(W/k_B T_K)^2$ , where  $W$  is the bare conduction-electron bandwidth. This enhancement factor is huge—about  $10^4 - 10^6$  for moderately to strongly renormalized heavy-fermion semimetals. As another example, the enhanced Berry curvature near the Fermi energy can be probed through the spontaneous Hall effect<sup>17</sup>.

The second category of experimental signatures are distinct for the Kondo-driven nodal-line phase. As one example, the nodal lines lead to a non-trivial Berry phase of any closed loop perpendicular to the mirror plane. The resulting characteristic signatures in quantum oscillations for such a strongly correlated setting are considerably more challenging to probe than their weakly correlated counterparts<sup>39-41</sup>. However, in materials with moderate mass enhancement (as we will identify below), these experiments are expected to be feasible. As another example, the drumhead surface states will lead to distinct spectroscopic signatures. They can, as in weakly correlated systems<sup>42</sup>, in principle be probed by quasiparticle-interference measurements via scanning tunneling microscopy (STM).

We turn next to demonstrating how our approach guides the search for new correlated topological materials. CeSbTe is a well-known square-net material that hosts  $f$ -electrons<sup>31</sup>. However, it exhibits an antiferromagnetic order at  $T_N = 2.7$  K, which breaks time-reversal symmetry. Still, the amount of entropy that has been measured in such a temperature range suggests that the system will be strongly correlated if it is tuned to a paramagnetic state. Thus, tuning these systems into their paramagnetic ground state is suggested as a means of realizing the Kondo-driven topological semimetal we have advanced here.

Guided by the demonstrated cooperation between strong correlations and space group symmetry, we propose two new materials of SG 129, CeRh<sub>2</sub>Ga<sub>2</sub> and CePt<sub>2</sub>Si<sub>2</sub>, to realize the Kondo-driven semimetal phase. Both remain paramagnetic and otherwise electronically disordered down to the lowest temperature of somewhat below 2 K<sup>43,44</sup> that has been experimentally measured, and both have strong correlations as inferred from their moderately enhanced specific heat (see Supplementary Information). Moreover, both show semimetallic behavior: Their resistivity as a function of temperature [Fig. S2(a)(b)] behaves similarly as the well-established heavy-fermion semimetals Ce<sub>3</sub>Bi<sub>4</sub>Pd<sub>3</sub> and CeNiSn, respectively [Fig. S2(c)(d)]. For CePt<sub>2</sub>Si<sub>2</sub>, the  $spd$  electronic structure, determined by  $f$ -core DFT calculations (see Methods), are displayed in Fig. 2(c). As can be seen, the symmetry of SG 129 dictates the existence of Dirac nodes at the  $X$ ,  $M$ ,  $R$  and  $A$  points, which are located away from the Fermi energy. The results for CeRh<sub>2</sub>Ga<sub>2</sub> are similar (see Supplemen-

tary Information). The DFT-calculated electronic structure is expected to apply well above the Kondo temperature. Below their respective Kondo temperatures, the approach we have advanced here suggests that they will realize Kondo-driven topological semimetals. The precise nature of the renormalized band structure requires the construction of tight-binding representations of the DFT-derived band structure as well as *ab initio* input of the Kondo couplings; we reserve such a study for a future work.

Studies of these materials set the stage to search for additional strongly correlated semimetals. In the case of a nonzero inversion-symmetry-breaking term  $\Delta$ , corresponding to SG 31,  $\text{Ce}_2\text{Au}_3\text{In}_5$  is a candidate heavy-fermion material that is known not to order down to the lowest measured temperature (2 K)<sup>45</sup>. We propose it as a candidate material to realize the Weyl-Kondo nodal-line semimetal advanced here.

Emergent low-energy excitations can already develop for intermediate correlations, when the correlation strength is comparable to the noninteracting bandwidth. They will also be subject to space-group symmetry constraints. As such, our approach raises the prospect that electron correlations can act in concert with crystalline symmetries in intermediately correlated systems. Materials that have been explored in this regime include the uranium-based magnetic kagome heavy fermion metals<sup>19</sup> and the binary kagome metals<sup>20,21</sup>. More generally, we can expect our approach to provide a means for identifying hitherto-unknown correlated topological phases in a variety of correlated electron settings.

In conclusion, we have advanced a design principle for strong correlations to cooperate with space group symmetry and drive correlated topological solids. Strong correlations lead to low-energy emergent excitations, which are subject to the constraints of the space group symmetry for topological phases. We have tested this approach in Kondo lattice models whose space group symmetries may promote different kinds of electronic degeneracies. In nonsymmorphic and non-centrosymmetric square-net systems, we have theoretically validated the approach by demonstrating novel Weyl-Kondo nodal-line semimetals in both two and three dimensions. The approach has allowed us to propose specific correlated materials to realize the correlation-driven topological semimetals, and we have described how *ab initio* electronic-structure calculations and experimental data support our identification. Our findings illustrate the potential of the proposed design principle to guide the search for new correlated topological metals in a broad range of strongly

correlated quantum materials.

---

1. Keimer, B. & Moore, J. E. The physics of quantum materials. *Nat. Phys.* **13**, 1045 (2017).
2. Paschen, S. & Si, Q. Quantum phases driven by strong correlations. *Nat. Rev. Phys.* **3**, 9 (2021).
3. Armitage, N. P., Mele, E. J. & Vishwanath, A. Weyl and Dirac semimetals in three-dimensional solids. *Rev. Mod. Phys.* **90**, 015001 (2018).
4. Cano, J. & Bradlyn, B. Band representations and topological quantum chemistry. *Annu. Rev. Condens. Matter Phys.* **12**, 225–246 (2021).
5. Bradlyn, B., Elcoro, L., Cano, J., Vergniory, M. G., Wang, Z., Felser, C., Aroyo, M. I. & Bernevig, B. A. Topological quantum chemistry. *Nature* **547**, 298–305 (2017).
6. Cano, J., Bradlyn, B., Wang, Z., Elcoro, L., Vergniory, M. G., Felser, C., Aroyo, M. I. & Bernevig, B. A. Building blocks of topological quantum chemistry: Elementary band representations. *Phys. Rev. B* **97**, 035139 (2018).
7. Po, H. C., Vishwanath, A. & Watanabe, H. Symmetry-based indicators of band topology in the 230 space groups. *Nat. Commun.* **8**, 50 (2017).
8. Watanabe, H., Po, H. C., Zaletel, M. P. & Vishwanath, A. Filling-enforced gaplessness in band structures of the 230 space groups. *Phys. Rev. Lett.* **117**, 096404 (2016).
9. Schaffer, R., Lee, E. K.-H., Yang, B.-J. & Kim, Y. B. Recent progress on correlated electron systems with strong spin-orbit coupling. *Rep. Prog. Phys.* **79**, 094504 (2016).
10. Huh, Y., Moon, E.-G. & Kim, Y. B. Long-range Coulomb interaction in nodal-ring semimetals. *Phys. Rev. B* **93**, 035138 (2016).
11. Maciejko, J. & Fiete, G. A. Fractionalized topological insulators. *Nat. Phys.* **11**, 385 (2015).
12. Rachel, S. & Le Hur, K. Topological insulators and Mott physics from the Hubbard interaction. *Phys. Rev. B* **82**, 075106 (2010).
13. Lai, H.-H., Greife, S. E., Paschen, S. & Si, Q. Weyl-Kondo semimetal in heavy-fermion systems. *Proc. Natl. Acad. Sci. U.S.A.* **115**, 93–97 (2018).
14. Greife, S. E., Lai, H.-H., Paschen, S. & Si, Q. Weyl-Kondo semimetals in nonsymmorphic systems. *Phys. Rev. B* **101**, 075138 (2020).
15. Greife, S. E., Lai, H.-H., Paschen, S. & Si, Q. Extreme topological tunability of Weyl-Kondo semimetal to Zeeman coupling. *arXiv:2012.15841* .

16. Dzsaber, S., Prochaska, L., Sidorenko, A., Eguchi, G., Svagera, R., Waas, M., Prokofiev, A., Si, Q. & Paschen, S. Kondo insulator to semimetal transformation tuned by spin-orbit coupling. *Phys. Rev. Lett.* **118**, 246601 (2017).
17. Dzsaber, S., Yan, X., Taupin, M., Eguchi, G., Prokofiev, A., Shiroka, T., Blaha, P., Rubel, O., Grefe, S. E., Lai, H.-H., Si, Q. & Paschen, S. Giant spontaneous Hall effect in a nonmagnetic Weyl-Kondo semimetal. *Proc. Natl. Acad. Sci. U.S.A.* **118**, e2013386118 (2021).
18. Dzsaber, S., Zocco, D. A., McCollam, A., Weickert, F., McDonald, R., Taupin, M., Yan, X., Prokofiev, A., Tang, L. M. K., Vlaar, B., Winter, L. E., Jaime, M., Si, Q. & Paschen, S. Controlling electronic topology in a strongly correlated electron system. *arXiv:1906.01182* .
19. Asaba, T., Ivanov, V., Thomas, S. M., Savrasov, S. Y., Thompson, J. D., Bauer, E. D. & Ronning, F. Colossal anomalous Nernst effect in a correlated noncentrosymmetric kagome ferromagnet. *Sci. Adv.* **7**, eabf1467 (2021).
20. Kang, M., Ye, L., Fang, S., You, J.-S., Levitan, A., Han, M., Facio, J. I., Jozwiak, C., Bostwick, A., Rotenberg, E., Chan, M. K., McDonald, R. D., Graf, D., Kaznatcheev, K., Vescovo, E., Bell, D. C., Kaxiras, E., van den Brink, J., Richter, M., Prasad Ghimire, M., Checkelsky, J. G. & Comin, R. Dirac fermions and flat bands in the ideal kagome metal FeSn. *Nat. Mater.* **19**, 163 (2020).
21. Yao, M., Lee, H., Xu, N., Wang, Y., Ma, J., Yazyev, O., Xiong, Y., Shi, M., Aeppli, G. & Soh, Y. Switchable Weyl nodes in topological kagome ferromagnet Fe<sub>3</sub>Sn<sub>2</sub>. *arXiv:1810.01514* .
22. Morimoto, T. & Nagaosa, N. Weyl Mott insulator. *Sci. Rep.* **6**, 19853 (2016).
23. Wagner, N., Ciuchi, S., Toschi, A., Trauzettel, B. & Sangiovanni, G. Resistivity exponents in 3d Dirac semimetals from electron-electron interaction. *Phys. Rev. Lett.* **126**, 206601 (2021).
24. Fu, L., Kane, C. L. & Mele, E. J. Topological insulators in three dimensions. *Phys. Rev. Lett.* **98**, 106803 (2007).
25. Chiu, C.-K. & Schnyder, A. P. Classification of reflection-symmetry-protected topological semimetals and nodal superconductors. *Phys. Rev. B* **90**, 205136 (2014).
26. Bian, G., Chang, T.-R., Sankar, R., Xu, S.-Y., Zheng, H., Neupert, T., Chiu, C.-K., Huang, S.-M., Chang, G., Belopolski, I., Sanchez, D. S., Neupane, M., Alidoust, N., Liu, C., Wang, B., Lee, C.-C., Jeng, H.-T., Zhang, C., Yuan, Z., Jia, S., Bansil, A., Chou, F., Lin, H. & Hasan, M. Z. Topological nodal-line fermions in spin-orbit metal PbTaSe<sub>2</sub>. *Nat. Commun.* **7**, 10556 (2016).
27. Bian, G., Chang, T.-R., Zheng, H., Velury, S., Xu, S.-Y., Neupert, T., Chiu, C.-K., Huang, S.-M., Sanchez, D. S., Belopolski, I., Alidoust, N., Chen, P.-J., Chang, G., Bansil, A., Jeng, H.-T., Lin, H. &

- Hasan, M. Z. Drumhead surface states and topological nodal-line fermions in  $\text{TlTaSe}_2$ . *Phys. Rev. B* **93**, 121113 (2016).
28. Chan, Y.-H., Chiu, C.-K., Chou, M. Y. & Schnyder, A. P.  $\text{Ca}_3\text{P}_2$  and other topological semimetals with line nodes and drumhead surface states. *Phys. Rev. B* **93**, 205132 (2016).
29. Young, S. M. & Kane, C. L. Dirac semimetals in two dimensions. *Phys. Rev. Lett.* **115**, 126803 (2015).
30. Schoop, L. M., Ali, M. N., Straßer, C., Topp, A., Varykhalov, A., Marchenko, D., Duppel, V., Parkin, S. S. P., Lotsch, B. V. & Ast, C. R. Dirac cone protected by non-symmorphic symmetry and three-dimensional Dirac line node in  $\text{ZrSiS}$ . *Nat. Commun.* **7**, 11696 (2016).
31. Schoop, L. M., Topp, A., Lippmann, J., Orlandi, F., Muechler, L., Vergniory, M. G., Sun, Y., Rost, A. W., Duppel, V., Krivenkov, M., Sheoran, S., Manuel, P., Varykhalov, A., Yan, B., Kremer, R. K., Ast, C. R. & Lotsch, B. V. Tunable Weyl and Dirac states in the nonsymmorphic compound  $\text{CeSbTe}$ . *Sci. Adv.* **4**, eaar2317 (2018).
32. Muechler, L., Topp, A., Queiroz, R., Krivenkov, M., Varykhalov, A., Cano, J., Ast, C. R. & Schoop, L. M. Modular arithmetic with nodal lines: Drumhead surface states in  $\text{ZrSiTe}$ . *Phys. Rev. X* **10**, 011026 (2020).
33. Klemenz, S., Schoop, L. & Cano, J. Systematic study of stacked square nets: From Dirac fermions to material realizations. *Phys. Rev. B* **101**, 165121 (2020).
34. Nica, E. M., Yu, R. & Si, Q. Glide reflection symmetry, Brillouin zone folding, and superconducting pairing for the  $P4/nmm$  space group. *Phys. Rev. B* **92**, 174520 (2015).
35. Wu, W., Jiao, Y., Li, S., Sheng, X.-L., Yu, Z.-M. & Yang, S. A. Hourglass Weyl loops in two dimensions: Theory and material realization in monolayer  $\text{GaTeI}$  family. *Phys. Rev. Materials* **3**, 054203 (2019).
36. Aeppli, G. & Fisk, Z. Kondo insulators. *Comm. Condensed Matter Phys.* **16**, 155 (1992).
37. Dzero, M., Sun, K., Galitski, V. & Coleman, P. Topological Kondo insulators. *Phys. Rev. Lett.* **104**, 106408 (2010).
38. Nikolić, P. Two-dimensional heavy fermions on the strongly correlated boundaries of Kondo topological insulators. *Phys. Rev. B* **90**, 235107 (2014).
39. Li, C., Wang, C. M., Wan, B., Wan, X., Lu, H.-Z. & Xie, X. C. Rules for phase shifts of quantum oscillations in topological nodal-line semimetals. *Phys. Rev. Lett.* **120**, 146602 (2018).
40. Yang, H., Moessner, R. & Lim, L.-K. Quantum oscillations in nodal line systems. *Phys. Rev. B* **97**, 165118 (2018).

41. Kwan, Y. H., Reiss, P., Han, Y., Bristow, M., Prabhakaran, D., Graf, D., McCollam, A., Parameswaran, S. A. & Coldea, A. I. Quantum oscillations probe the fermi surface topology of the nodal-line semimetal CaAgAs. *Phys. Rev. Research* **2**, 012055 (2020).
42. Stuart, B., Choi, S., Kim, J., Muechler, L., Queiroz, R., Oudah, M., Schoop, L., Bonn, D. & Burke, S. Quasiparticle interference observation of the topologically non-trivial drumhead surface state in ZrSiTe. *arXiv:2010.00070*.
43. Anand, V. K., Adroja, D. T., Bhattacharyya, A., Klemke, B. & Lake, B. Kondo lattice heavy fermion behavior in CeRh<sub>2</sub>Ga<sub>2</sub>. *J. Phys. Condens. Matter* **29**, 135601 (2017).
44. Gignoux, D., Schmitt, D., Zerguine, M., Ayache, C. & Bonjour, E. Magnetic properties of a new Kondo lattice compound: CePt<sub>2</sub>Si<sub>2</sub>. *Phys. Lett. A* **117**, 145–149 (1986).
45. Galadzhun, Y. V., Hoffmann, R.-D., Pöttgen, R. & Adam, M. Complex three-dimensional Au<sub>3</sub>In<sub>5</sub> polyanions in Ln<sub>2</sub>Au<sub>3</sub>In<sub>5</sub> (Ln = Ce, Pr, Nd, Sm). *J. Solid State Chem.* **148**, 425–432 (1999).
46. Bhattacharjee, A., Coqblin, B., Raki, M., Forro, L., Ayache, C. & Schmitt, D. Anisotropy of transport properties in the Kondo compound CePt<sub>2</sub>Si<sub>2</sub>: experiments and theory. *J. Phys. (Paris)* **50**, 2781–2793 (1989).
47. Nakamoto, G., Takabatake, T., Fujii, H., Minami, A., Maezawa, K., Oguro, I. & Menovsky, A. Crystal growth and characterization of the Kondo semimetal CeNiSn. *J. Phys. Soc. Jpn.* **64**, 4834–4840 (1995).
48. Kresse, G. & Hafner, J. Ab initio molecular dynamics for open-shell transition metals. *Phys. Rev. B* **48**, 13115–13118 (1993).
49. Kresse, G. & Furthmüller, J. Efficiency of ab-initio total energy calculations for metals and semiconductors using a plane-wave basis set. *Comput. Mater. Sci.* **6**, 15–50 (1996).
50. Perdew, J. P., Burke, K. & Ernzerhof, M. Generalized gradient approximation made simple. *Phys. Rev. Lett.* **77**, 3865–3868 (1996).
51. Kresse, G. & Joubert, D. From ultrasoft pseudopotentials to the projector augmented-wave method. *Phys. Rev. B* **59**, 1758–1775 (1999).
52. Hobbs, D., Kresse, G. & Hafner, J. Fully unconstrained noncollinear magnetism within the projector augmented-wave method. *Phys. Rev. B* **62**, 11556–11570 (2000).
53. Nesterenko, S., Avzuragova, V., Tursina, A. & Kaczorowski, D. Structural peculiarities and magnetic properties of a novel cerium gallide CeRh<sub>2</sub>Ga<sub>2</sub>. *J. Alloys Compd.* **717**, 136–140 (2017).

## **Acknowledgments**

Work at Rice has been supported by the Air Force Office of Scientific Research under Grant No. FA9550-21-1-0356 (C.S. and Q.S.), the National Science Foundation under Grant No. DMR-1920740 (L.C.) and the Robert A. Welch Foundation Grant No. C-1411 (H.H.). The majority of the computational calculations have been performed on the Shared University Grid at Rice funded by NSF under Grant EIA-0216467, a partnership between Rice University, Sun Microsystems, and Sigma Solutions, Inc., the Big-Data Private-Cloud Research Cyberinfrastructure MRI-award funded by NSF under Grant No. CNS-1338099, and the Extreme Science and Engineering Discovery Environment (XSEDE) by NSF under Grant No. DMR170109. M.G.V. acknowledges the support from the Spanish Ministry of Science and Innovation Grant No. PID2019-109905GB-C21. Work at Los Alamos was carried out under the auspices of the U.S. Department of Energy (DOE) National Nuclear Security Administration under Contract No. 89233218CNA000001, and was supported by LANL LDRD Program. J.C. acknowledges the support of the National Science Foundation under Grant No. DMR-1942447 and the support of the Flatiron Institute, a division of the Simons Foundation. A.P. and S.P. acknowledge the funding from the Austrian Science Fund (project No. 29279-N27). Four of us (S.G., S. P., J. C. and Q.S.) acknowledge the hospitality of the Aspen Center for Physics, which is supported by NSF grant No. PHY-1607611.

## **Author contributions**

Q.S., J.C. and S. P. conceived the research. L.C., C.S., H.H., S.E.G., J.C. and Q.S. carried out theoretical model studies. A.P. and S.P. identified candidate materials for the proposed correlated topological semimetals. M.G.V. performed DFT calculations. L.C., C.S., H.H., J.C. and Q.S. wrote the manuscript, with inputs from all authors.

## **Competing interests**

The authors declare no competing interests.

## **Additional information**

Correspondence and requests for materials should be addressed to Q.S. (qmsi@rice.edu), J.C. (jennifer.cano@stonybrook.edu) and S.P. (paschen@ifp.tuwien.ac.at)

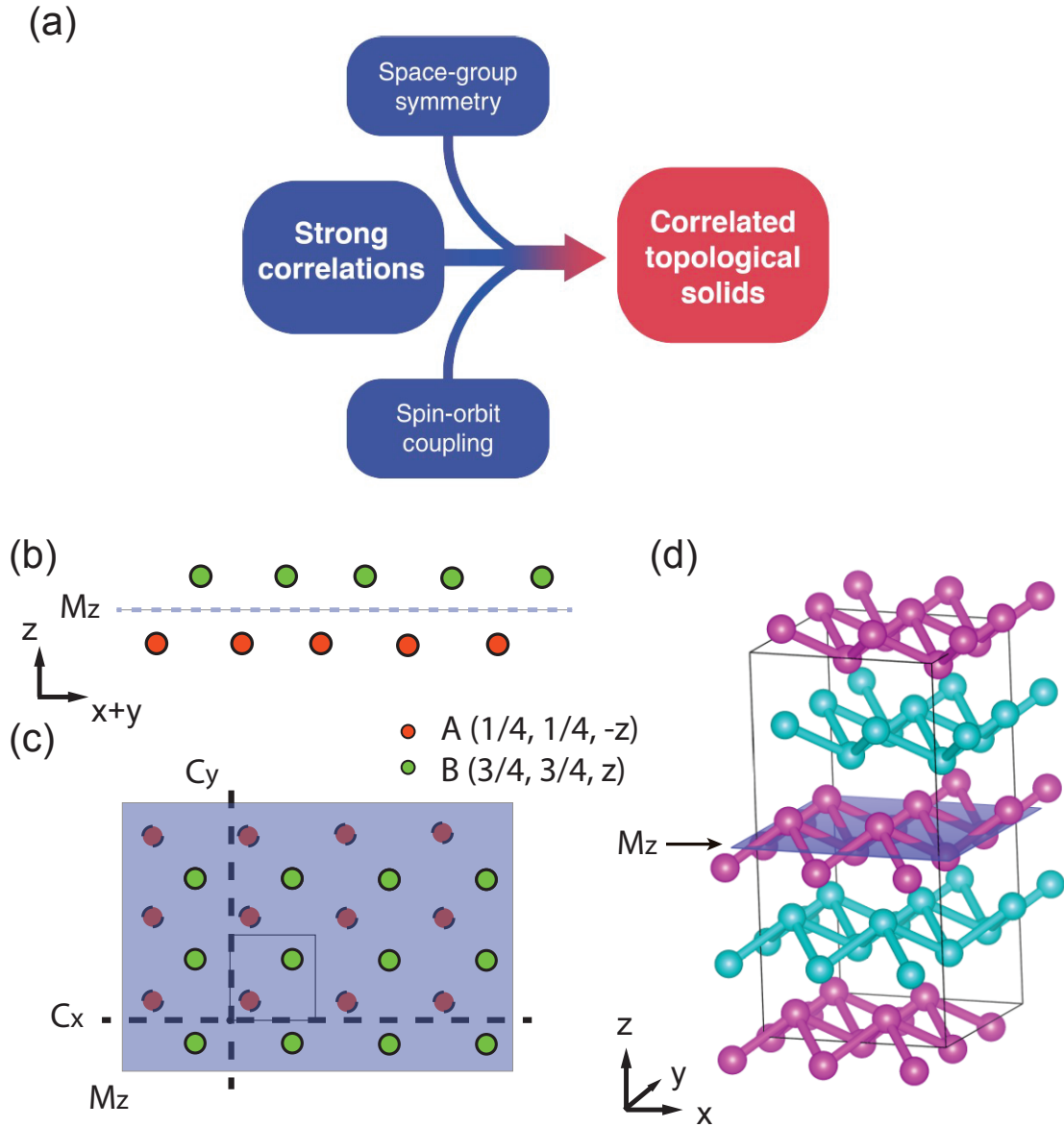


FIG. 1. **Design principle and space-group symmetry.** **a**, The proposed cooperation between strong correlations and space-group symmetry in realizing correlated topological states. **b, c**, The lattice structure of the square-net layer with sublattices  $A$ ,  $B$  on Wyckoff position  $2c$ . Also shown are the mirror ( $M_z$ ) and screw ( $C_x$  and  $C_y$ ) nonsymmorphic symmetries. **d**,  $AA$  stacking of the square-net layers into a 3D structure.

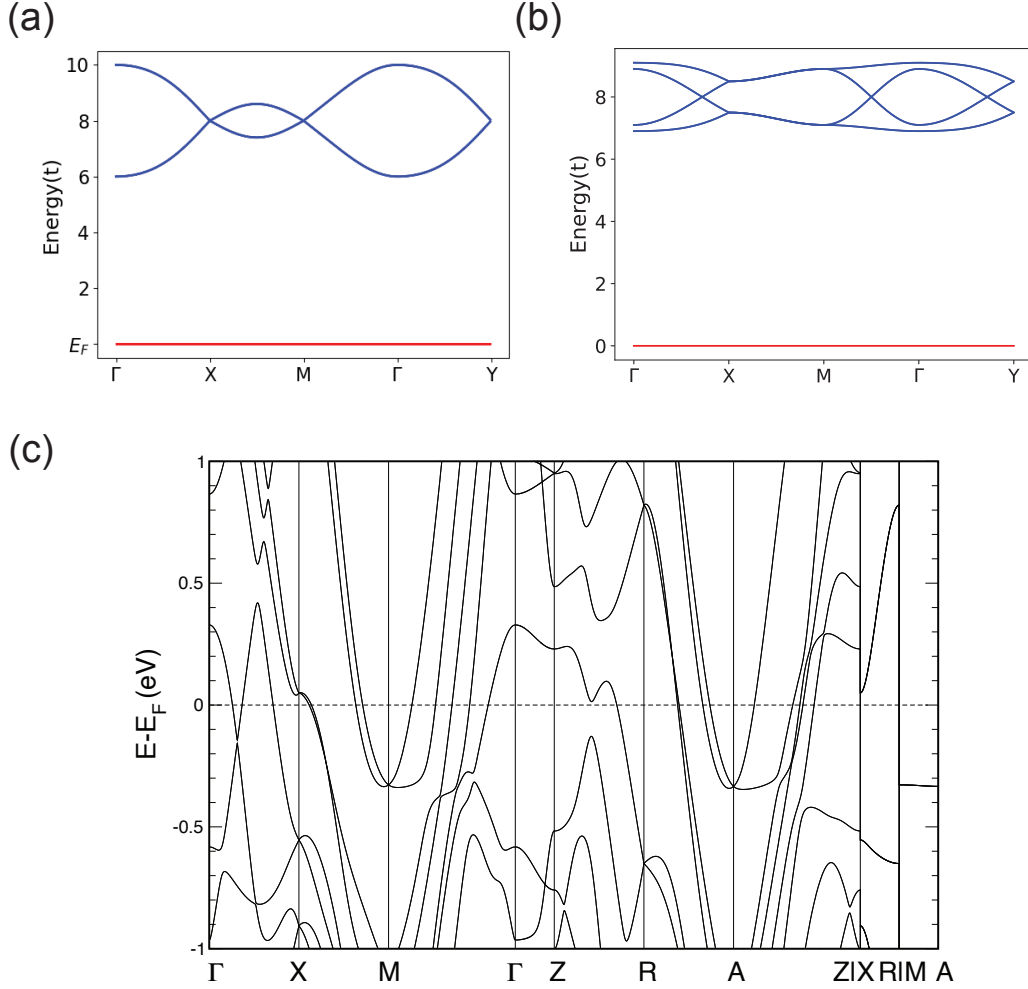
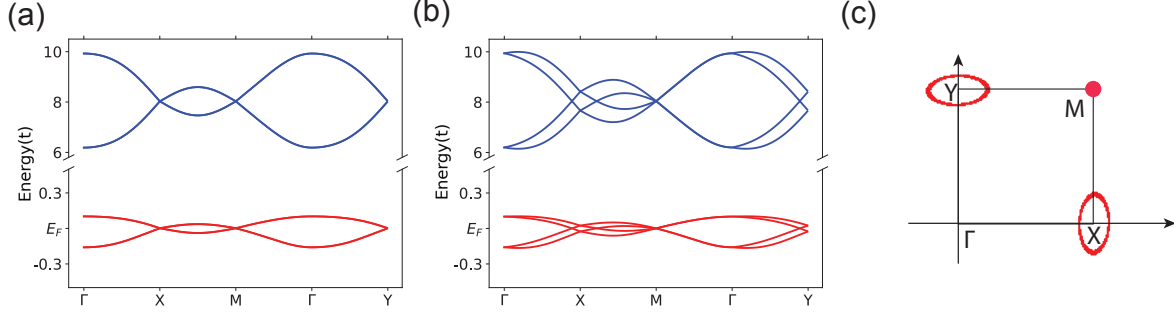


FIG. 2. **Electronic structure in the absence of Kondo effect.** **a**, Dispersion of a 2D square net with  $(t_1, t_2, t^{SO}) = (1, 0, 0.6)$ . The line at  $E_F$  illustrates the localized electrons. The four-fold degeneracies of the conduction bands occur at high symmetry points  $X, Y, M$  away from the Fermi energy. **b**, Dispersion of the 3D-stacked square net without either inversion symmetry breaking or SOC. The parameters are  $(t_1, t_2, t_z^1, t_z^2, \Delta_z) = (1, 0.4, 0.3, 0.3, 0.8)$ . **c**, Bandstructure of the conduction *spd*-electrons of  $\text{CePt}_2\text{Si}_2$ , as determined by *f*-core DFT calculations. Symmetry-dictated Dirac nodes appear at  $X$  and  $M$  (and  $R$  and  $A$ ) away from the Fermi energy, as captured by the model dispersions of **a** and **b**.



**FIG. 3. Renormalized electronic structure of a 2D square net in the presence of Kondo effect.** **a**, The renormalized dispersion, including for the Kondo-driven composite fermions (the lower red part), at  $\Delta = 0$ . The Kondo-driven Dirac nodes are pinned to  $E_F$  at the high symmetry points  $X, Y, M$ . Here, the parameters are  $(V, E_d, t_1, t_2, t^{SO}, \mu, r, l) = (6.8, -6, 1, 0, 0.6, -7.529, 0.285, -6.500)$ . **b**, The dispersion of the Kondo-driven Weyl nodal-line semimetal. **c**, The Kondo-driven Weyl nodal lines (the red lines) encircle high symmetry points  $X$  and  $Y$ . Here  $\Delta = 0.4$ , and the other parameters are  $(V, E_d, t_1, t_2, t^{SO}, \mu, r, l) = (6.8, -6, 1, 0, 0.6, -7.564, -0.286, -6.500)$ .

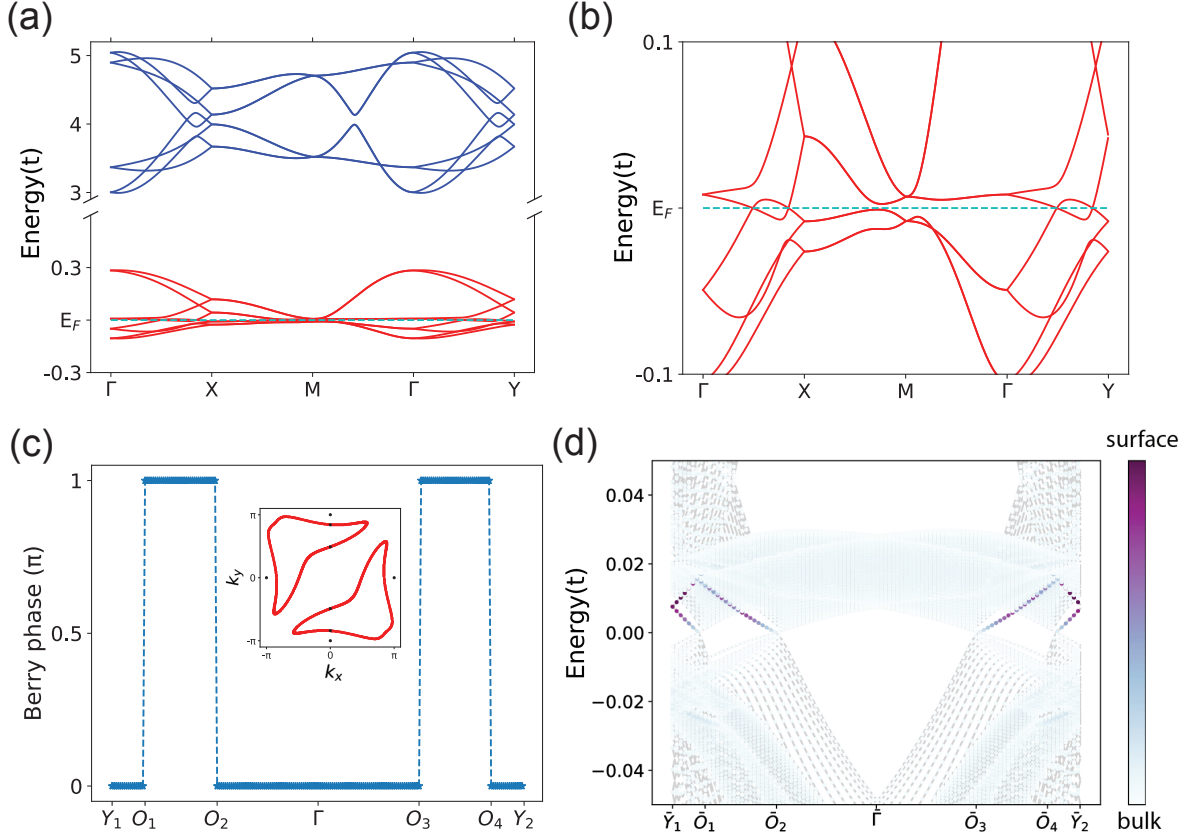


FIG. 4. **Renormalized electronic structure of 3D stacked square-nets with broken inversion symmetry in the presence of Kondo effect.** **a**, The renormalized dispersion, including for the Kondo-driven composite fermions (the lower red part), within the  $k_z = 0$  plane. Here  $V = 3$ , with the other parameters being  $(t_1, t_2, \Delta, t_z^1, t_z^2, \Delta_z, m_z) = (1, 0.4, 0.4, 0.3, 0.3, 0.8, 0.08)$  and  $(E_d, \mu, r_1, r_2, l_1, l_2) = (-2, -3.730, 0.498, 0.374, -2.820, -2.294)$ . **b**, The zoomed-in dispersion of the Kondo-driven composite fermions. **c**, The Berry phase (in the  $z$ -direction) of the Kondo-driven Weyl nodal lines for fixed  $k_x = 0$ ;  $O_{1,2,3,4}$  mark the points of intersection with the nodal lines [Fig. S1(c)]. Inset: the Kondo-driven Weyl nodal lines in the  $k_z = 0$  plane. **d**, Kondo driven drumhead surface states. Shown here is the momentum-resolved surface density of states for the spectrum close to Fermi energy on the (001) surface along  $Y_1(0, -\pi)$  to  $Y_2(0, \pi)$ . A bar atop a momentum represents its projection onto the surface.

## Methods

**The periodic Anderson model** The PAM in 2D takes the following form:

$$\mathcal{H} = \mathcal{H}_d + \mathcal{H}_{cd} + \mathcal{H}_c, \quad (3)$$

where the  $d$ -fermion is the physically localized  $f$  electrons specified by

$$\mathcal{H}_d = E_d \sum_{i,\sigma} d_{i\sigma}^\dagger d_{i\sigma} + U \sum_i n_{i\uparrow}^d n_{i\downarrow}^d. \quad (4)$$

The  $f$ -electrons in the atomic limit are characterized by an energy level  $E_d$  and an energy penalty  $U$  from the Coulomb interaction if the orbital is doubly occupied. The hybridization term, which describes the Kondo coupling between the conduction electrons and the local moments, is given by

$$\mathcal{H}_{cd} = V \sum_{i\sigma} \left( d_{i\sigma}^\dagger c_{i\sigma} + h.c. \right), \quad (5)$$

where  $c_{i\sigma}$  denotes the light  $spd$  conduction electrons,  $V$  represents the Kondo hybridization. The conduction electrons are described by  $\mathcal{H}_c = \sum_{\mathbf{k}} \Psi_{\mathbf{k}}^\dagger H_c(\mathbf{k}) \Psi_{\mathbf{k}}$ , where  $\Psi_{\mathbf{k}}^T = (c_{\mathbf{k}\uparrow A}, c_{\mathbf{k}\downarrow A}, c_{\mathbf{k}\uparrow B}, c_{\mathbf{k}\downarrow B})$ , and

$$\begin{aligned} H_c(\mathbf{k}) = & t_1 \cos \frac{k_x}{2} \cos \frac{k_y}{2} \tau_x + t_2 (\cos k_x + \cos k_y) + t^{SO} (\sin k_x \sigma_y - \sin k_y \sigma_x) \tau_z \\ & + \Delta \sin\left(\frac{k_x - k_y}{2}\right) \tau_x \sigma_z, \end{aligned} \quad (6)$$

where  $\tau = (\tau_x, \tau_y, \tau_z)$ 's and  $\sigma = (\sigma_x, \sigma_y, \sigma_z)$ 's are Pauli matrices acting on the (A,B) sublattice and spin spaces respectively. For definiteness, we consider the lattice model with tight-binding hopping terms between the nearest ( $t_1$ ) and next-nearest ( $t_2$ ) terms, an SOC ( $t^{SO}$ ) term, and an inversion-symmetry-breaking ( $\Delta$ ) term. The first three terms contain all the symmetry-allowed components up to the next-nearest neighbor, describing an effective  $s$ -orbital model on Wyckoff position  $2c$  with both time reversal symmetry ( $\mathcal{T}$ ) and inversion symmetry ( $\mathcal{I}$ ). The presence of both  $\mathcal{T}$  and  $\mathcal{I}$  ensure each band is doubly degenerate with states  $|g\rangle$  and  $\mathcal{T}\mathcal{I}|g\rangle$ . In addition, the symmetries include the glide mirror symmetry  $\{M_z|\frac{1}{2}\frac{1}{2}\}$  (Fig. 1(b)(c)) and two screw symmetries  $\{C_{2x}|\frac{1}{2}0\}$  and  $\{C_{2y}|0\frac{1}{2}\}$  (where  $\{C_{ni}|\mathbf{t}\} = n$ -fold rotation along axis  $i$  + fractional translation  $\mathbf{t}$  as depicted in Fig. 1(c)). They enforce additional crossings at high symmetry points  $X$ ,  $Y$  and  $M^{29}$ . The fourth term has the form of  $\Delta \sin(\frac{k_x - k_y}{2}) \tau_x \sigma_z$ . It breaks the inversion symmetry of  $p4/nmm$ , while preserving its mirror symmetry<sup>29,35</sup>. The quarter-filling case we examine corresponds to one electron per site. We consider the realistic regime of parameters corresponding to the limit of

strong coupling,  $U \rightarrow \infty$ , and with the  $d$ -electron level being sufficiently deep compared to the energy of the conduction-electron bands (*i.e.*, for sufficiently negative  $E_d$ ), in which the system is in the Kondo limit. We analyze the problem using an auxiliary-boson representation of the correlated  $d$ -electrons that leads to a set of saddle-point equations, as described in the Supplementary Information.

The PAM in 3D is given in Eq. 1. For simplicity, we have chosen an  $s$ - and  $p$ -orbital stacking and set the  $s$  and  $p$  orbitals to couple with the  $d$ -electrons with the same hybridization strength, although the nature of the resulting topological semimetal phase is generic. Further details of our analysis is described in the Supplementary Information.

***f*-core DFT calculations** The electronic structure calculations were performed with the  $f$  states removed from the pseudo-potential to model the band structure. The SOC was taken into account. Further details can be found in the Supplementary Information.

**Data availability** The data that support the findings of this study are available from the corresponding author upon reasonable request.

# Supplementary Information

## Additional data for the Kondo-driven nodal line in 3D

In Fig. 4 of the main text, we showed the renormalized electronic structure for the 3D square net along high-symmetry directions within the  $k_z = 0$  plane. Here, we plot the bands along high-symmetry directions in the entire 3D Brillouin zone. The renormalized band structure is shown in Fig. S1(a) along the path connecting high symmetry points as can be seen through Fig. S1(b). Except for the Weyl line in the  $k_z = 0$  plane, the heavy bands are fully gapped across the 3D Brillouin zone.

## Saddle point equations

We describe the auxiliary-boson method in this section. In the 2D square-net model, we first fix the electron filling to be one per site

$$n_d + n_c = 1, \quad (\text{S1})$$

with

$$n_d = \frac{1}{N_u} \sum_{i,\sigma} d_{i\sigma}^\dagger d_{i\sigma}, \quad (\text{S2})$$

$$n_c = \frac{1}{N_u} \sum_{i,\sigma} c_{i\sigma}^\dagger c_{i\sigma}, \quad (\text{S3})$$

where  $N_u$  counts the total number of sites.

In the infinite- $U$  limit, the localized  $d$ -electrons can be represented as  $d_{i\sigma}^\dagger = b_i f_{i\sigma}^\dagger$  with local constraint

$$b_i^\dagger b_i + \sum_{\sigma} f_{i\sigma}^\dagger f_{i\sigma} = 1. \quad (\text{S4})$$

This constraint rules out the double occupancy entirely. At the saddle point, the auxiliary bosons condense, with  $b_i \rightarrow \langle b_i \rangle = r$ . We further introduce a uniform Lagrangian multiplier  $l$  to enforce the local constraint in Eq. S4, which gives rise to the saddle-point Hamiltonian:

$$\mathcal{H}_s = \mathcal{H} + l \left( \frac{1}{N_u} \sum_{i,\sigma} f_{i\sigma}^\dagger f_{i\sigma} + r^2 - 1 \right) - \mu \frac{1}{N_u} \sum_{i,\sigma} n_{i\sigma}^c, \quad (\text{S5})$$

where  $\mu$  is the chemical potential. The saddle point equations are

$$\sum_{\sigma} (V \langle d_{\sigma}^\dagger f_{\sigma} \rangle + h.c.) - 2rl = 0, \quad (\text{S6})$$

$$\sum_{\sigma} \langle f_{\sigma}^\dagger f_{\sigma} \rangle - r^2 = 1. \quad (\text{S7})$$

Together with the filling constraint Eq. S1, we can self-consistently determine the variational parameters  $(\mu, r, l)$ .

We apply the same auxiliary-boson method to the 3D stacked square net with a saddle-point Hamiltonian

$$\begin{aligned}
H = & H_c^{3D} + r_1 V \sum_{\sigma} (s_{\sigma}^{\dagger} f_{\sigma}^1 + h.c.) + E_d \sum_{\sigma} f_{\sigma}^{1\dagger} f_{\sigma}^1 \\
& + r_2 V \sum_{\sigma} (p_{\sigma}^{\dagger} f_{\sigma}^2 + h.c.) + E_d \sum_{\sigma} f_{\sigma}^{2\dagger} f_{\sigma}^2 \\
& + l_1 \left( \sum_{\sigma} f_{\sigma}^{1\dagger} f_{\sigma}^1 + r_1^2 - 1 \right) + l_2 \left( \sum_{\sigma} f_{\sigma}^{2\dagger} f_{\sigma}^2 + r_2^2 - 1 \right) \\
& - \mu \sum_{\sigma} (s_{\sigma}^{\dagger} s_{\sigma} + p_{\sigma}^{\dagger} p_{\sigma}),
\end{aligned} \tag{S8}$$

where  $f_{\sigma}^1$  and  $f_{\sigma}^2$ ,  $r_1$  and  $r_2$ ,  $l_1$  and  $l_2$  represent the auxiliary fermions, condensed auxiliary bosons and Lagrangian multipliers for each layer.

The saddle point equations are

$$\frac{1}{N_u} \sum_{\sigma} (V \langle s_{\sigma}^{\dagger} f_{\sigma}^1 \rangle + h.c.) - 2r_1 l_1 = 0, \tag{S9}$$

$$\frac{1}{N_u} \sum_{\sigma} \langle f_{\sigma}^{1\dagger} f_{\sigma}^1 \rangle - r_1^2 = 1, \tag{S10}$$

$$\frac{1}{N_u} \sum_{\sigma} (V \langle p_{\sigma}^{\dagger} f_{\sigma}^2 \rangle + h.c.) - 2r_2 l_2 = 0, \tag{S11}$$

$$\frac{1}{N_u} \sum_{\sigma} \langle f_{\sigma}^{2\dagger} f_{\sigma}^2 \rangle - r_2^2 = 1. \tag{S12}$$

The filling is still fixed to be one per site.

### **CeRh<sub>2</sub>Ga<sub>2</sub> and CePt<sub>2</sub>Si<sub>2</sub> as strongly correlated semimetals**

The two candidate materials we have identified, CeRh<sub>2</sub>Ga<sub>2</sub> and CePt<sub>2</sub>Si<sub>2</sub>, show properties that are characteristic of strongly correlated semimetals. Their strong correlations are signaled by the large enhancement of the specific heat from the typical values of weakly correlated metals. The electronic specific-heat coefficient  $C/T$  reaches 130 and 80 mJ/mol K<sup>2</sup>, respectively<sup>43,44</sup> (*i.e.* about 100 times the effective mass of weakly correlated bulk metals). Their semimetal nature is captured by the resistivity as a function of temperature, respectively shown in Fig. S2(a)(b) for the two compounds<sup>43,46</sup>, which behaves similarly as Fig. S2(c)(d), respectively, for the well-established heavy-fermion semimetals Ce<sub>3</sub>Bi<sub>4</sub>Pd<sub>3</sub> and CeNiSn<sup>16,47</sup>. In all cases, the temperature dependence of the resistivity is neither activated, as a fully-gapped system would be, nor showing a giant  $T^2$ -dependent component at low temperatures with a positive temperature slope, as a typical

heavy-fermion metal would be. This feature is accompanied by the relatively large magnitude of the resistivity.

### Further details and additional results of the DFT calculations

The electronic structure calculations were performed using the Vienna ab initio simulation package (VASP)<sup>48,49</sup> with the Perdew, Burke and Ernzerhof (PBE) generalized gradient approximation for the exchange correlation potential<sup>50</sup>. The  $f$  states were removed from the pseudo-potential to model the band structure. The interaction between the ion cores and valence electrons was described by the projector augmented-wave method<sup>51</sup>. The Hamiltonian contained the scalar relativistic corrections, and the SOC was taken into account by the second variation method<sup>52</sup>.

The calculation for CeRh<sub>2</sub>Ga<sub>2</sub> is in principle more difficult, given that the Rh- and Ga-site displacive disorder in the existing materials has been reported<sup>53</sup>. To get a qualitative understanding, we have carried out  $f$ -core DFT calculations but ignoring the disorder, with the Rh and Ga atoms fully assigned to the 2c and 2a sites, respectively. The results are shown in Fig. S3.

### Specific heat

To calculate the low- $T$  specific heat, we focus on the linear-dispersion regime where we can approximate the dispersion  $\epsilon_{\mathbf{k}} = \epsilon_{\mathbf{k}_{\perp}} = \hbar v^* k_{\perp}$ . Here,  $\mathbf{k} = (k_{\parallel}, \mathbf{k}_{\perp})$  represents the decomposition of the wave vector into the components parallel and perpendicular to the nodal line;  $\mathbf{k}_{\perp}$  itself has two components.

The specific heat becomes

$$\begin{aligned}
c_v &= \frac{\partial}{\partial T} \int_{-\infty}^{+\infty} \frac{d\epsilon}{(2\pi)^3} \epsilon \rho(\epsilon) f(\epsilon) \\
&= \frac{\partial}{\partial T} \int_{-\infty}^{+\infty} \frac{d\epsilon}{(2\pi)^3} \epsilon \frac{2K\pi\epsilon}{(\hbar v^*)^2} \frac{1}{e^{\epsilon/k_B T} + 1} \\
&= \frac{K}{(2\pi)^3} \frac{\partial}{\partial T} \int_0^{2\pi} d\theta \int_0^{k_K} dk_{\perp} \frac{2\pi(\hbar v^*)^3 k_{\perp}^2}{(\hbar v)^2} \frac{1}{e^{\hbar v^* k_{\perp}/k_B T} + 1} \\
&= \frac{K}{2\pi} \frac{9\zeta(3)}{2} k_B \left( \frac{k_B T}{\hbar v^*} \right)^2,
\end{aligned} \tag{S13}$$

where  $K$  is the length of the nodal line and  $\zeta(3) \approx 1.202$ . So the specific heat per unit volume is

$$c_v = \Gamma T^2, \tag{S14}$$

$$\Gamma = \frac{K}{2\pi} \frac{9\zeta(3)}{2} \frac{(k_B)^3}{(\hbar v^*)^2}. \tag{S15}$$

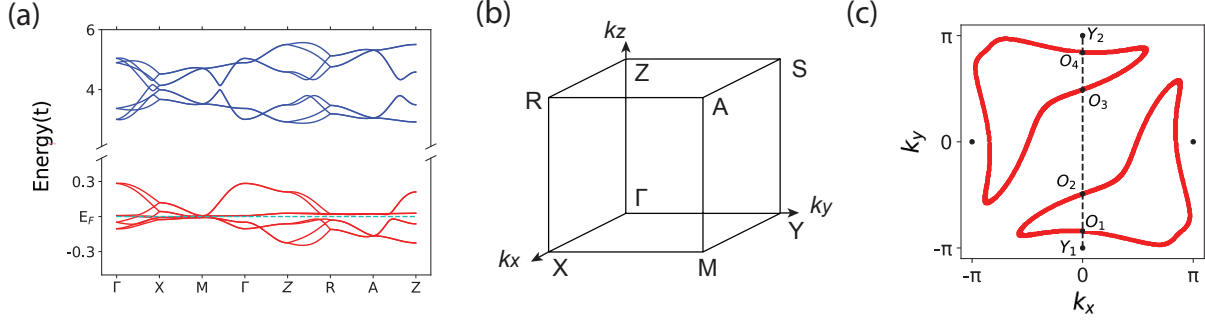


**FIG. S1. Renormalized dispersion in the 3D-stacked square-net model over an extended region of the Brillouin zone.** **a**, Renormalized dispersion across both the  $k_z = 0$  and  $k_z = \pi$  planes with the same parameters as shown in Fig. 4. The heavy bands (lower red part) are fully gapped when  $k_z \neq 0$ . **b**, The 3D Brillouin zone with high symmetry points  $\Gamma = (0, 0, 0)$ ,  $X = (\pi, 0, 0)$ ,  $Y = (0, \pi, 0)$ ,  $M = (\pi, \pi, 0)$ ,  $Z = (0, 0, \pi)$ ,  $R = (\pi, 0, \pi)$ ,  $S = (0, \pi, \pi)$  and  $A = (\pi, \pi, \pi)$ . **c**, The Kondo-driven Weyl nodal lines, which intersect with the dashed  $k_x = 0$  line from  $Y_1 = (0, -\pi, 0)$  to  $Y_2 = (0, \pi, 0)$  at  $O_1$ ,  $O_2$ ,  $O_3$  and  $O_4$ .

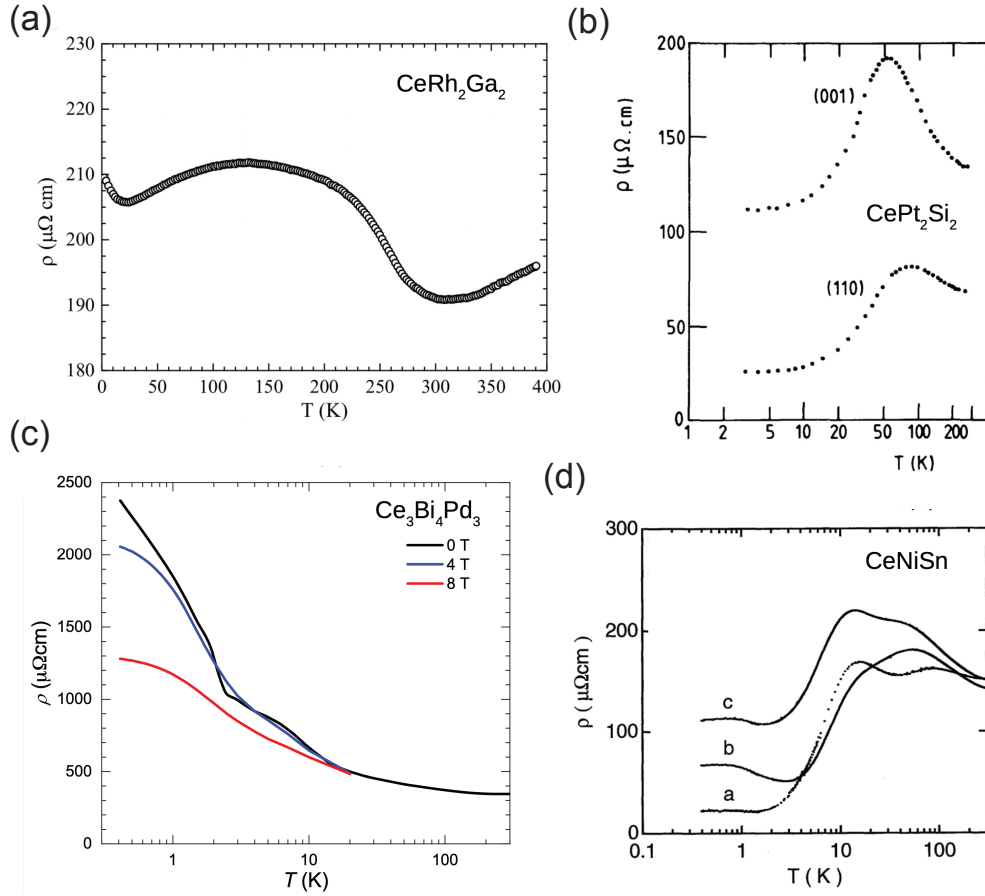


FIG. S2. **Semimetal transport of Ce-based square-net materials.** Resistivity ( $\rho$ ) vs. temperature ( $T$ ) of **a**,  $\text{CeRh}_2\text{Ga}_2$ <sup>43</sup>, **b**,  $\text{CePt}_2\text{Si}_2$ <sup>46</sup>, **c**,  $\text{Ce}_3\text{Bi}_4\text{Pd}_3$ <sup>16</sup>, and **d**,  $\text{CeNiSn}$ <sup>47</sup>.

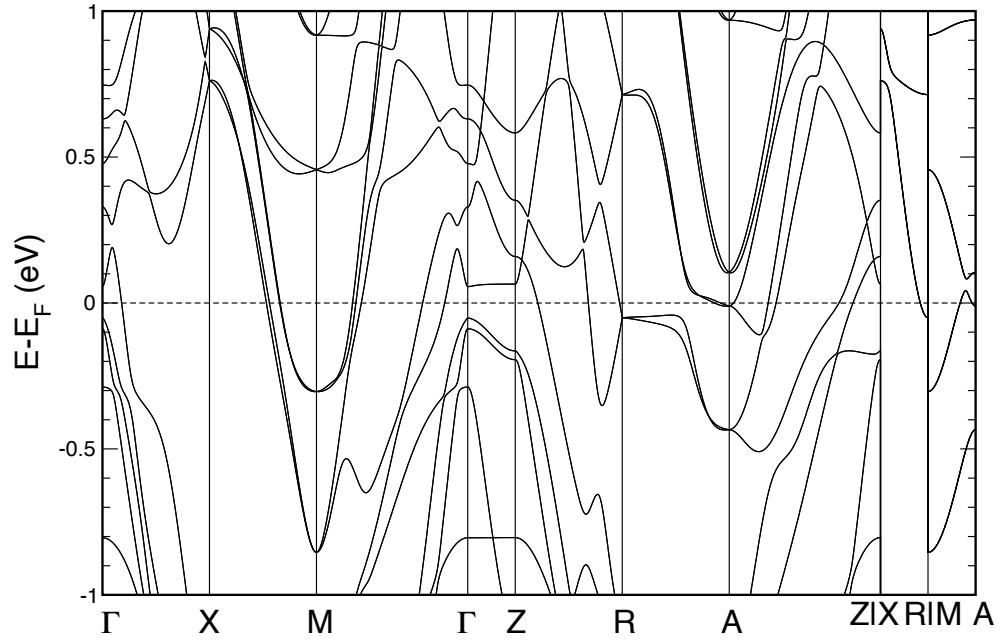


FIG. S3. **DFT results for CeRh<sub>2</sub>Ga<sub>2</sub>.** Shown are the results derived from ignoring the site-displacive disorder of the Rh and Ga atoms.